# Estimation of radiative capture $^{13}$B($n$, $\gamma_{0+1}$)$^{14}$B reaction rate in the modified potential cluster model*

A.S. Tkachenko[1†] N.A. Burkova[2] B.M. Yeleusheva[2] S.B. Dubovichenko[1‡]

[1]Fesenkov Astrophysical Institute, 050020, Almaty, Kazakhstan
[2]al-Farabi Kazakh National University, 050040, Almaty, Kazakhstan

**Abstract:** We discuss current attempts to employ the modified potential cluster model to describe the available experimental data on the $^{13}$B($n$, $\gamma_{0+1}$)$^{14}$B total cross-sections. The estimated results of the $M1$ and $E1$ transitions from the $n^{13}$B scattering states to the ground and first excited states of $^{14}$B are presented. The 1$^{st}$ resonance at $E_x$ = 1. 275 MeV ($1^+$) is revealed in both the cross-section and reaction rate. Within the variation in the asymptotic constant, a thermal cross-section interval of 5.1 – 8.9 mb is proposed. Based on the theoretical total cross-sections at energies of 0.01 eV to 5 MeV, we calculate the reaction rate in the temperature range of 0.01 to 10$T_9$. The ignition $T_9$ values of the $^{13}$B($n$, $\gamma_{0+1}$)$^{14}$B reaction depending on a neutron number density $\bar{n}_n$ of ~ $10^{22}$ cm$^{-3}$ are determined. The radiative neutron capture reaction rates on the boron $^{10\text{-}13}$B and carbon $^{12\text{-}14}$C isotopes are compared.

**Keywords:** radiative neutron capture, $^{14}$B nucleus, total cross-sections, reaction rate, potential cluster model, $r$-process.

**DOI:** 10.1088/1674-1137/acee55

## I. INTRODUCTION

Conventional studies on $r$-processes focus on producing heavy unstable nuclei. Among the thousands of publications, one may be impressed by the recent reviews [1–3].

The interesting aspects of the current study lie in the area of $r$-processes that occur with light 1$p$-shell nuclei and are motivated by the concepts suggested in Refs. [4– 6]. Kajino *et al.* suggested networks for primordial nucleosynthesis in inhomogeneous Big Bang models in Ref. [4] and their further extension to the evolution of light elements in cosmic rays [5].

More than 20 years ago, Terasawa *et al*. raised the problem of the role of light neutron-rich nuclei ($Z$ < 10) in $r$-process nucleosynthesis in supernovae [6]. In particular, we are interested in the possible branching of boron and carbon chains leading to the formation of heavier isotopes up to oxygen for the development of a primordial chain starting from $^7$Li (see Fig. 6 in Ref. [7] and our illustration in Fig. 1).

Further development of sensitivity studies on the ($n$, $\gamma$) reactions running through the neutron-rich boron $^{11-14}$B and $^{12-19}$C carbon isotopes was achieved by Sasaqui *et al*. [7], and these reactions have been included in heavy nuclei network production. Almost all reaction rates for the boron chains used in these model calculations were taken from [8], and their uncertainties were estimated to be at least a factor of two [7]. It turned out that only the $^{13}$B($n$, $\gamma$)$^{14}$B process on boron isotopes exhibited zero impact on heavy element production.

We suggest a new estimation of the $^{13}$B($n$, $\gamma$)$^{14}$B reaction rate within the modified potential cluster model (MPCM) approach, which significantly differs from the results of Ref. [8]. Therefore, we can provide reasons for revising the conclusions of [7] on the negligible role of the $^{13}$B($n$, $\gamma$)$^{14}$B reaction in heavy nuclei network production.

A comparative analysis of the reaction rates of the processes in Fig. 1 is a way of defining the contribution of the $^{13}$B($n$, $\gamma$)$^{14}$B reaction in the boron-carbon-nitrogen network. Our early MPCM research on neutron radiative capture reactions relevant to those in Fig. 1 is provided in the following references: the $^{10}$B($n$, $\gamma$)$^{11}$B reaction is examined in Ref. [9], the reaction chain $^{11}$B($n$, $\gamma$)$^{12}$B($n$, $\gamma$)$^{13}$B is considered in Refs. [10, 11, 12], we investigated $^{12}$C($n$, $\gamma$)$^{13}$C in Ref. [13] and $^{13}$C($n$, $\gamma$)$^{14}$C in Ref. [14], $^{14}$C($n$, $\gamma$)$^{15}$C is not yet published, and research on the $^{15}$N($n$, $\gamma$)$^{16}$N process is presented in Ref. [15].

For the reaction $^{16}$O($n$, $\gamma$)$^{17}$O, the measured cross-section and its rate, calculated in the direct reaction capture

Received 21 June 2023; Accepted 9 August 2023; Published online 10 August 2023

* Supported by the Ministry of Science and Higher Education of the Republic of Kazakhstan (AP09259174)

† E-mail: tkachenko.alessya@gmail.com

‡ E-mail: dubovichenko@mail.ru

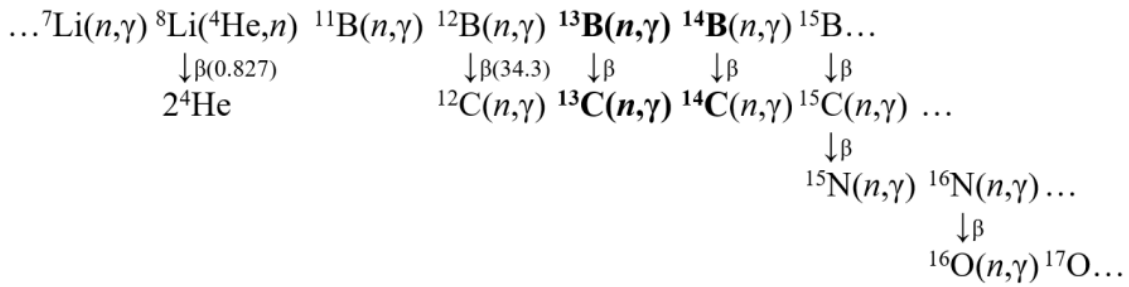


**Fig. 1.** Part of the nuclear reaction network responsible for producing light elements in primordial nucleosynthesis (from [4–6]).

model, are presented in the recent Ref. [16]. There are no data on the $^{14}$B($n$, γ)$^{15}$B and $^{16}$N($n$, γ)$^{17}$N reaction rates to date.

Experimental study of the $^{13}$B($n$, γ)$^{14}$B reaction is presented using the only measurement of the neutron breakup of the $^{15}$B isotope via Coulomb dissociation performed in inverse kinematics [17]. The total cross-section of $^{13}$B($n$, γ)$^{14}$B is derived from the Coulomb breakup of $^{15}$B and is very tentative. Therefore, theoretical model calculations are in high demand to fill the information gap on the $^{13}$B($n$, γ)$^{14}$B reaction in boron chains as in Fig. 1.

Another problem concerns the lack of well-defined information on the spectral structure of $^{14}$B required to apply the MPCM. We use current data on the $^{14}$B spectrum [18], as opposed to previous data from an earlier review [19], to classify the possible multipole structure of the corresponding cross-sections of present and future interest.

Interestingly, the reactions $^{13}$B($n$, γ)$^{14}$B and $^{13}$C($n$, γ)$^{14}$C are isobar-analogous, and the latter is examined in detail in Ref. [14]. Although $^{14}$B and $^{14}$C are not mirror nuclei, the Young diagrams reveal several common features of orbital symmetry. We exploit this fact while classifying the allowed and forbidden states (FS) in the discrete and continuum spectra of $n$ + $^{13}$B channels.

Within the MPCM, the total cross-sections of $^{13}$B($n$, γ)$^{14}$B radiative capture onto the ground state (GS) and first excited state (ES) of $^{14}$B are calculated, as well as the reaction rates in the interval $0.01T_9$ – $10T_9$. Based on the reaction rate interval, we evaluate the balance between $^{14}$B synthesis via the radiative neutron capture reaction $^{13}$B($n$, γ)$^{14}$B and $^{13}$B decay inhibiting this synthesis.

This paper is organized as follows. Sec. II contains the MPCM presentation of $^{14}$B in the $n$ + $^{13}$B channel. In Sec. III, the total cross-sections of the $^{13}$B($n$, $\gamma_{0+1}$)$^{14}$B reaction are considered. In Sec. IV, we present the $n^{13}$B radiative capture reaction rate and compare the neutron radiative capture rates on $^{10\text{-}13}$B and $^{12\text{-}14}$C isotopes. We outline the conclusions in Sec. V. Appendix A includes the numerical values of the $n^{13}$B reaction rate, and Appendix B illustrates the computational procedure accuracy of the reaction rate calculations.

## II. MPCM PRESENTATION OF $^{14}$B IN THE $n$+$^{13}$B CHANNEL

### A. Structure of states for the n$^{13}$B system

We preface the calculations of the reaction cross-sections with an analysis of the $^{14}$B spectrum data, following Ref. [18]. The spectrum of selected levels of the $^{14}$B nucleus is shown in Fig. 2. The structure of the bound ground state $J^{\pi}$, $T = 2^{-}$, 2 is assigned as a combination of two main orbital components: $\psi_{GS} = \alpha_S |S\rangle + \alpha_D |D\rangle + ...$, where the corresponding weights are $\alpha_S = 0.71(5)$ and $\alpha_D = 0.17(5)$. In the present calculations, we consider the $S$-component only. As for the excited $J^{\pi} = 1^{-}$ state, it is found to be the dominant $S$-component with a weight $\alpha_S = 0.94(20)$.

Now, let us comment on the resonance states in the spectrum of $^{14}$B. The 1$^{st}$ resonance can be associated with the spin-mixed $^{3+5}P_1$ wave at the energy $E_{\text{c.m.}} = 0.305(20)$ MeV because $J^{\pi} = 3/2^{-}$ for $^{13}$B and $J^{\pi} = 2^{-}$ for $^{14}$B. Radiative neutron capture from this state proceeds via the $E1$ transition to the ground $^{5}S_2$ and excited $^{3}S_1$ states.

The 2$^{nd}$ resonance has $J^{\pi} = 3^{-}$ and may be excited at 0.41 MeV as a $^{3+5}D_2$ state so that only the $E2$ transition may occur. Because we are operating within the long-wave approximation for the electromagnetic interaction Hamiltonian here and henceforth, we do not consider the $E2$ or $M2$ transitions if selection rules do not forbid the more strong $E1$ and $M1$ processes.

The 3$^{rd}$ resonance with $J^{\pi} = 2^{-}$ may be excited at 0.89(7) MeV in the $^{5}S_2$ or $^{3+5}D_2$ scattering waves. From the $^{5}S_2$ scattering wave, the $M1$ transition to the GS is allowed, but we assume that owing to the large width $\Gamma_{\text{c.m.}}$ =1.0(5) MeV, this resonance does not practically affect the total capture cross-section if this resonance is considered a spin-mixed $^{3+5}D_2$ wave.

The 4$^{th}$ resonance at an excitation energy of 2.08(5) MeV is defined as the $J^{\pi} = 4^{-}$ state, but its width is unknown. It may be matched to a $^{5}D_3$ scattering wave, leading to the $E2$ transition, and is not considered in present calculations.

The position of the 5$^{th}$ resonance in the spectrum is defined at 4.06(5) MeV, with a width of 1.2(5) MeV and

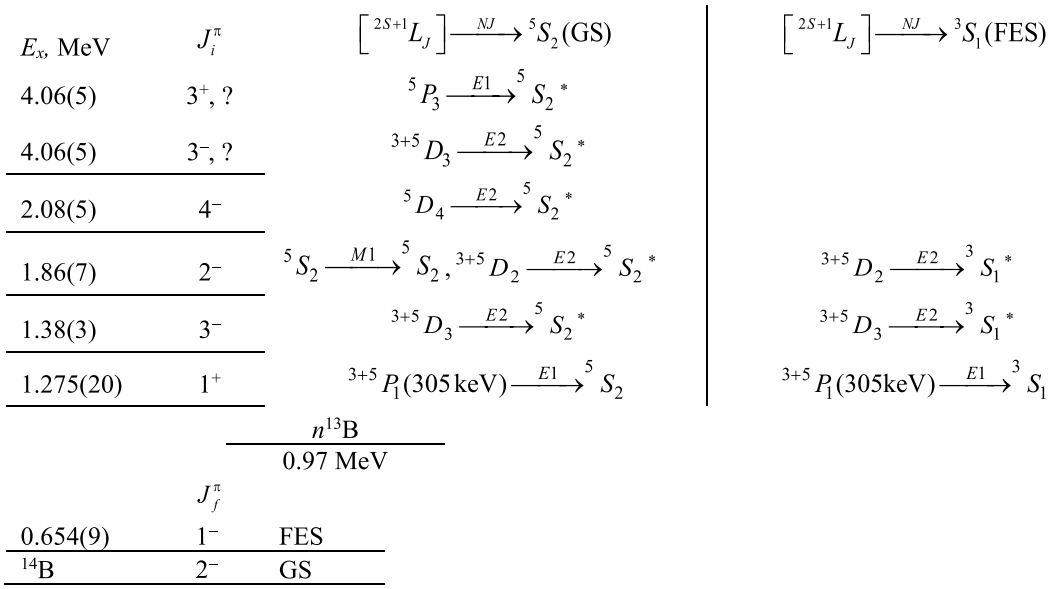


**Fig. 2.** Spectrum of the $^{14}$B nucleus in MeV [18]. * indicates the transitions we do not consider.

a total spin $J = 3$, but the parity is unknown [18]. We assume a positive parity for this level and construct a resonance potential for the $^5P_3$ scattering wave. The $^5P_3$ state leads to the $E1$ transition to the $^5S_2$ ground state of $^{14}$B. Its effect on the total cross-section is weak owing to its large width. If a negative parity is assumed, this state is the analog of the 2$^{nd}$ resonance state mentioned above.

We do not denote two other levels in the spectrum at energies of 2.32(4) MeV and 2.97(4) MeV because only their energies are known [18]. Transitions labeled as *not considered* in Fig. 2 may be assumed as perspectives for future study of the $^{13}$B($n$, $\gamma$)$^{14}$B reaction when new experimental data on the $^{14}$B spectrum are available.

### B. Calculation formalism and interaction potentials

The cross-sections of $E1$ and $M1$ capture to the GS are provided by the following transition amplitudes:

$$^{3+5}P_1(305\text{ keV}) \xrightarrow{E1} {}^5S_2,\quad {}^5P_3 \xrightarrow{E1} {}^5S_2,\quad {}^{3+5}P_2 \xrightarrow{E1} {}^5S_2,$$
$$^3P_0 \xrightarrow{E1} {}^5S_2,\quad {}^5S_2 \xrightarrow{M1} {}^5S_2. \tag{1}$$

For the cross-sections of $E1$ and $M1$ capture to the ES of $^{14}$B, these transition amplitudes are

$$^3P_1(305\text{ keV}) \xrightarrow{E1} {}^3S_1, {}^3P_0 \xrightarrow{E1} {}^3S_1, {}^3P_2 \xrightarrow{E1} {}^3S_1, {}^3S_1 \xrightarrow{M1} {}^3S_1. \tag{2}$$

The calculation of the corresponding cross-sections is performed using the following formalism [20–23] adapted to the selected $E1$ and $M1$ transitions:

$$\sigma(N1, J_f) = \frac{2\pi e^2}{3\hbar^2}\left(\frac{\mu K}{k}\right)^3 \sum_{L_i, J_i} (2J_i + 1)\cdot B^2(N1)\cdot I^2_{NJ}(k, J_f, J_i), \tag{3}$$

$$B^2(E1) = \frac{25}{m^2_{^{13}\text{B}}}, I_{EJ}(k, J_f, J_i) = \left\langle \chi_f \left| r^J \right| \chi_i \right\rangle, \tag{4}$$

$$B^2(M1) = 3\left(\frac{\hbar}{m_0 c}\right)^2 \left[\frac{\mu_n}{m_n} - \frac{\mu_{^{13}\text{B}}}{m_{^{13}\text{B}}}\right]^2,$$
$$I_{MJ}(k, J_f, J_i) = \left\langle \chi_f \left| r^{J-1} \right| \chi_i \right\rangle, \tag{5}$$

where $N1 = E1$ or $M1$, $\mu$ is the reduced mass in the $n$ + $^{13}$B channel, $K$ is the $\gamma$-quantum wave number, $K = E_\gamma/\hbar c$, $k$ is the relative motion wave number related to the non-relativistic kinetic energy as $E_{\text{c.m.}} = \hbar^2 k^2/2\mu$, $J_i$ and $J_f$ are the total angular momenta, the multipolarity is fixed as the dipole $J = 1$, and $I_{NJ}(k, J_f, J_i)$ are the radial matrix elements over the relative distance $r$. We use masses of $m_n$ = 1.00866491597 amu [24] and $m_{^{13}\text{B}}$ = 13.0177802 amu [25], and the constant $\hbar^2/m_0$ = 41.4686 MeV·fm$^2$, where $m_0$ is the atomic mass unit (amu). The magnetic moments in (5) are given in nuclear magneton $\mu_N$: $\mu_n$ = −1.9130$\mu_N$, and $\mu_{^{13}\text{B}}$ = 3.1778 $\mu_N$ [18, 19, 24, 25].

The radial functions $\chi_i$ and $\chi_f$ are the numerical solutions of the Schrodinger equation, with the central interaction potential of Gaussian type for a fixed combination of angular momenta $JLS$,

$$V\left({}^{2S+1}L_J, r\right) = -V_0\left({}^{2S+1}L_J\right)\exp\left\{-\alpha\left({}^{2S+1}L_J\right)r^2\right\}, \tag{6}$$

where the potential parameters $V_0$ and α depend on the momenta $[{}^{2S+1}L_J]_{i,f}$ of the partial wave.

Following (1) and (2), the $S$ and $P$ waves provide the transition amplitudes in the initial continuum channel. The classification of orbital states using Young diagrams for the 14-nucleon system in the channel $A = 13 + 1$ proves that only $S$ waves are allowed, and $P$ waves also have a forbidden state [14]. Because there are no complete tables of the products of Young diagrams for a system with $A > 8$, we complement the symmetry analysis with the formalism of the translationally invariant shell model (TISM) [26, 27]. Therefore, we treat the option of the interaction potential with FS for $S$ waves.

The classification of orbital states using Young diagrams defines the optimization range of the potential depth $V_0$, *i.e.*, if FS exists in the given channel, the potential should be sufficiently deep to include this state. Otherwise, it may be shallow. Shallow potentials are appropriate for the description of scattering states without resonances and should give phase shifts close to zero [22, 23]. Deep non-resonance potentials should also provide the moderate energy dependence of phase shifts, which may be normalized according to the Levinson theorem (see details in [28]). In the case of resonance scattering states, the potential (6) should fit additional conditions – the reproduction of the resonance position $E_{\rm c.m.}$ and its width $\Gamma_{\rm c.m.}$ within the experimental uncertainties [11, 20].

We provide the potential parameters of the neutron scattering on $^{13}$B in Table 1.

Parameters of the $^{3+5}P_1$ wave potential are matched with the experimental values of the resonance position $E_{\rm c.m.}$ = 305(20) keV and width $\Gamma_{\rm c.m.}$ = 100(20) keV [18]. Calculations with potential No. 1 in Table 1 lead to $E_{\rm c.m.}$ = 305(1) keV and $\Gamma_{\rm c.m.}$ = 106(1) keV. The corresponding $^{3+5}P_1$ phase shift shown in Fig. 3 (red solid curve) reveals the resonant behavior and equals 270(1)° at 305 keV.

Non-resonance $^{3+5}P_2$, $^5P_3$, and $^3P_0$ waves are provided by potential No. 2 with FS from Table 1. Their phase shifts are normalized to 180(1)° according to the generalized Levinson theorem [28] (green dashed curve in Fig. 3).

For the non-resonance $S$-waves, we consider two variants of the interaction potentials. No. 3 from Table 1 refers to the case without FS and leads to a zero scattering $S$-phase shift. The inclusion of FS leads to a 180(1)° phase shift with the No. 4 parameters from Table 1. The construction of BS potentials is based on the demand to

**Table 1.** Parameters of the interaction potentials of the $n$ + $^{13}$B continuum.

| No. | $\{^{2S+1}L_J\}_i$ | $V_0$/ MeV | α/ fm$^{-2}$ |
|---|---|---|---|
| 1 | $^{3+5}P_1$ – resonance at 305 keV | 618.035 | 0.8 |
| 2 | $^{3+5}P_2$, $^5P_3$, $^3P_0$ – non-resonance | 1220.0 | 1.0 |
| 3 | $^5S_2$, $^3S_1$ – non-resonance | 0.0 | 0.0 |
| 4 | $^5S_2$ – non-resonance | 315.0 | 1.0 |

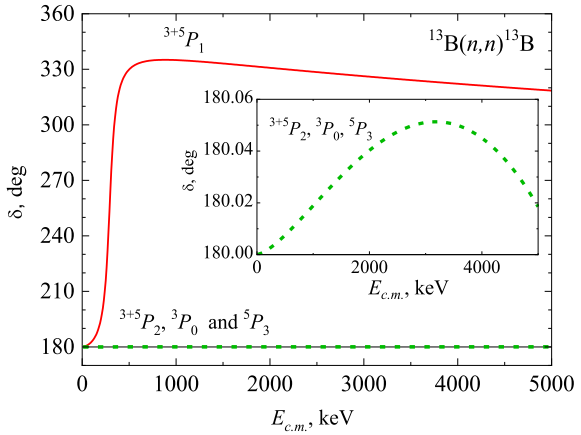


**Fig. 3.** (color online) $P$ wave phase shifts calculated in the MPCM with the parameters in Table 1: red solid curve – resonance $^{3+5}P_1$ wave, green dashed curve – non-resonance $^{3+5}P_2$, $^3P_0$, and $^5P_3$ waves.

reproduce the channel binding energy $E_b$ and match the corresponding asymptotic constant.

We use the well-known relation for the asymptotic normalizing coefficient $A_{\rm NC}$ and dimensionless asymptotic constant $C_W$ [22, 23],

$$C_W = \frac{A_{\rm NC}}{\sqrt{2k_0}} \cdot \frac{1}{\sqrt{S_f}}, \tag{7}$$

where the relative wave number $k_0$ is related to the binding energy $E_b = \hbar^2 k_0^2/2\mu$, and $S_f$ is the spectroscopic factor. Note that experimental data on $A_{\rm NC}$ usually found from the peripherical reactions alone with the spectroscopic factor $S_f$ are the input information for calculations of the theoretical values $C_W$. Ref. [29] reported the values $A_{\rm NC}$ = 0.73(10) fm$^{-1/2}$, obtained from measurements of the breakup cross-sections for the reaction $^9$Be($^{14}$B, $^{13}$B+$\gamma$)X at the National Superconducting Cyclotron Laboratory (NSCL), Michigan State University. Data on the spectroscopic factors $S_f$ = 0.71(19) [30] and $S_f$ = 0.66 [31] lead to the interval $0.52 \le S_f \le 0.9$. Consequently, the range for the dimensionless constant is $C_W$ = 1.40(38).

There are a number of phase shift equivalent potentials, which reproduce the channel binding energy exactly but lead to different radial wave functions. We exploit the $C_W$ constant to constrain the choice of the corresponding potential parameters. The asymptotic constant $C_W$ is not single-defined but has a range arising from experimental $A_{\rm NC}$ and $S_f$ values. There is also a variety of $V_0$ and α parameters, which provide the binding energy $E_b$ in the $n$ + $^{13}$B channel within the $C_W$ range. This is shown in the band for the corresponding cross-sections. For example, the details of the computing methods we use may be found in Ref. [20].

The parameters of the GS potentials of $^{14}$B in the $n$+$^{13}$B channel given in Table 2 reproduce a binding energy of

$E_b$ = −0.9700 MeV. The potentials of the GS Nos. 1, 2 and 3, 4 have nearly the same $C_W$ in pairs and allow us to present the effects of the FS.

The charge $R_{ch}$ and matter $R_m$ radii are calculated with these parameter sets according to the procedure in Ref. [32]. To calculate the $^{14}$B radii, we use the following input information: for $^{13}$B, the known values are $R_{ch}$($^{13}$B) = 2.48(3) fm and $R_m$($^{13}$B) = 2.41(5) fm [33]; the neutron matter radius is equal to the proton one, $R_m(n) = R_m(p)$ = 0.8414(19) fm [24], and the neutron charge radius $R_{ch}(n)$ = 0. The obtained results for $^{14}$B listed in Table 2 are in good agreement with the experimental values $R_{ch}$($^{14}$B) = 2.50(2) fm and $R_m$($^{14}$B) = 2.52(9) fm of Ref. [33].

The ES potentials of $^{14}$B in the $n^{13}$B channel with the parameters given in Table 3 reproduce the binding energy $E_b$ = 0.3160 MeV [32]. There is no data on $A_{NC}$ of the excited $1^-$ state; therefore, the corresponding $C_W$ constants in Table 3 as well as the $R_{ch}$ and $R_m$ radii may be recommended for future measurements. Along with Table 2, the potentials of the ES Nos. 1, 2 and 3, 4 are grouped in pairs for the same purpose to monitor the FS effects.

Note that the interaction potentials may depend on different diagrams for the same orbital $L$-waves of continuous and discrete spectra [34]. The $S$-wave potentials in Table 1 for the continuum and Tables 2 and 3 for the bound states are different. This is an important observation in the case of $M1$ transitions. Otherwise, the radial matrix elements in (5) at $J = 1$ are equal to zero owing to the orthogonality of the bound and scattering radial functions calculated in the same potential.

## III. TOTAL CROSS-SECTIONS OF THE $^{13}$B($n$, $\gamma$)$^{14}$B REACTION

The effect of the asymptotic $C_W$ constant on the total cross-sections for $^{13}$B($n$, $\gamma_0$)$^{14}$B capture to the GS of $^{14}$B is illustrated in Fig. 4 (a). The results of the calculations of the $E1$ and $M1$ partial cross-sections for potentials Nos. 1 ($C_W$ = 1.40) and 3 ($C_W$ = 2.10) from Table 2 and the scattering potentials from Table 1 are shown in comparison with the experimental data of [17]. Figure 4 (a) shows the total cross-sections in the linear energy scale up to 2.5 MeV to display the $^{3+5}P_1$ resonance at 305 keV.

Figure 4 (b) shows a wider range from $10^{-5}$ keV to 5 MeV relevant to the reaction rate calculation (see Sec. IV). The purpose of the results presented in Fig. 4 (b) is to answer the question of the role of the FS in the GS potentials from Table 2 arranged in pairs, *i.e.*, with or without FS at close $C_W$. The calculation results of the total cross-sections for the GS potentials with FS Nos. 2 ($C_W$ = 1.42) and 4 ($C_W$ = 2.15) are shown in Fig. 4 (b) by the green and magenta dotted curves, respectively.

We find good pairwise agreement with the results for potentials without FS. The slight variation is associated with a small difference in the values of $C_W$ and the scattering phase shifts of the $S$ potential with FS (No. 4 in Table 1) from exactly zero within 1 degree. At an energy of $10^{-5}$ keV, the cross-section value for the GS potential without FS No. 1 is equal to 8.05 mb, and for the GS with FS No. 2, it is equal to 8.36 mb. Similar results are obtained for the second potential with an FS. Therefore, we conclude that the presence or absence of FS does not affect the calculated total cross-section. The same consistent pattern is revealed in the ($n$, $\gamma_1$) capture calculations to the ES of $^{14}$B. Further results are presented only for potentials without FS.

To evaluate the thermal cross-sections, we use the standard approximation at energies from 10 meV to 1 keV,

$$\sigma_{ap}(\mu b) = \frac{A}{\sqrt{E_{c.m.}(keV)}}. \quad (8)$$

**Table 2.** Parameters of the GS potentials of $^{14}$B in the $n^{13}$B channel and calculated asymptotic constant $C_W$, $R_{ch}$, and $R_m$ radii.

| No. | $\{^{2S+1}L_J\}_i$ | $V_0$/ MeV | α/ fm$^{-2}$ | $C_W$ | $R_{ch}$/ fm | $R_m$/ fm |
|---|---|---|---|---|---|---|
| 1 | $^5S_2$ without FS | 19.0756 | 0.2 | 1.40(1) | 2.50 | 2.62 |
| 2 | $^5S_2$ with FS | 217.486 | 0.5 | 1.42(1) | 2.50 | 2.63 |
| 3 | $^5S_2$ without FS | 6.1237 | 0.04 | 2.10(1) | 2.52 | 2.81 |
| 4 | $^5S_2$ with FS | 49.262 | 0.1 | 2.15(1) | 2.52 | 2.84 |

**Table 3.** Parameters of the ES potentials of $^{14}$B in the $n^{13}$B channel and calculated asymptotic constant $C_W$, $R_{ch}$, and $R_m$ radii.

| No. | $\{^{2S+1}L_J\}_i$ | $V_0$/MeV | α/ fm$^{-2}$ | $C_w$ | $R_{ch}$/fm | $R_m$/fm |
|---|---|---|---|---|---|---|
| 1 | $^3S_1$ without FS | 15.75681 | 0.2 | 1.21(1) | 2.53 | 2.97 |
| 2 | $^3S_1$ with FS | 208.3937 | 0.5 | 1.22(1) | 2.53 | 2.98 |
| 3 | $^3S_1$ without FS | 4.27985 | 0.04 | 1.53(1) | 2.56 | 3.23 |
| 4 | $^3S_1$ with FS | 44.71865 | 0.1 | 1.56(1) | 2.56 | 3.27 |

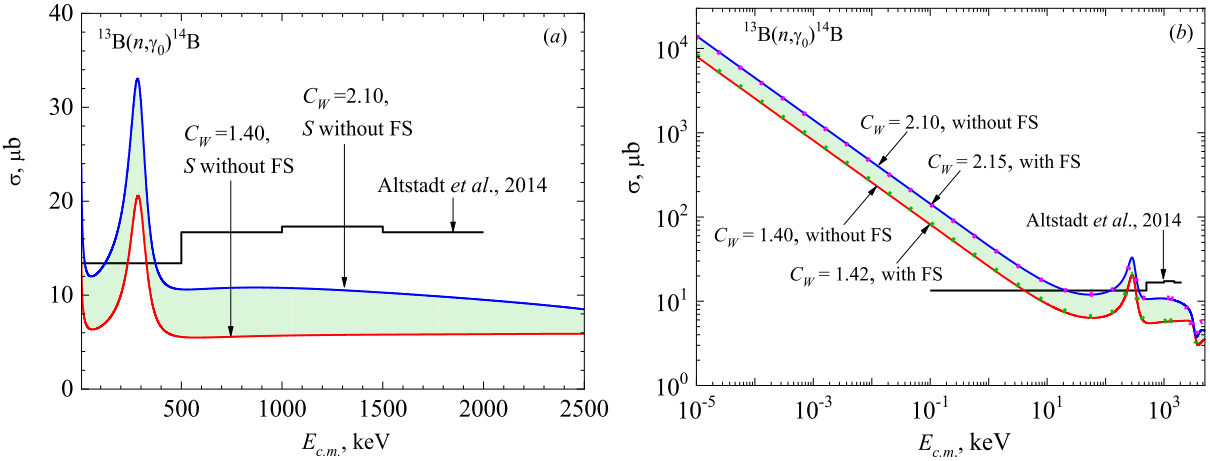


**Fig. 4.** (color online) Total cross-sections of $^{13}$B($n$, $\gamma_0$)$^{14}$B radiative capture to the GS of $^{14}$B with potentials from Tables 1 and 2. The histogram represents the experiment [17]. (*a*) Total cross-sections calculated without FS: red solid curve – potential No. 1 in Table 2 ($C_W$ = 1.40), blue solid curve – potential No. 3 in Table 2 ($C_W$ = 2.10). (*b*) Comparison of the total cross-sections calculated without and with FS: solid curves are the same as in Fig. 4 (a), green dotted curve – potential No. 2 in Table 2 ($C_W$ = 1.42), magenta dotted curve – potential No. 4 in Table 2 ($C_W$ = 2.15).

The value of the calculated cross-section $\sigma_{\text{theor}}(E)$ at $E_{\min}$ = 10 meV provides the constant $A$ = 25.46 μb·keV$^{1/2}$ for the red solid curve in Fig. 4 (b) ($C_W$ =1.40). Consequently, at a thermal energy of 25.3 meV, the cross-section $\sigma_{\text{therm}}$ = 5.1 mb. For the blue solid curve in Fig. 4 (b) ($C_W$ = 2.10), $A$ = 44.70 μb·keV$^{1/2}$ and $\sigma_{\text{therm}}$ = 8.9 mb.

The accuracy of the approximation (8) is defined by the relative difference between the cross-sections $\sigma_{\text{theor}}(E)$ and $\sigma_{\text{ap}}$ ($E$),

$$M(E) = \left|\left[\sigma_{\text{ap}}(E) - \sigma_{\text{theor}}(E)\right]\right| / \sigma_{\text{theor}}(E). \qquad (9)$$

$M$(1 keV) ≈ 0.2% for both cases of $C_W$ decreases with decreasing energy.

Figure 5 illustrates the input of the partial $E$1 and $M$1 cross-sections related to the set of amplitudes (1) of the ($n$, $\gamma_0$) process. The $M$1 transition from the $S$ wave determines the low-energy and thermal cross-sections. The $E$1 transition amplitudes define the higher energy region. The ($n$, $\gamma_1$) capture process reveals nearly the same partial structure (2).

Figure 6 illustrates the relative input of the ($n$, $\gamma_0$) and ($n$, $\gamma_1$) capture processes into the total cross-section. The dominance of the ($n$, $\gamma_0$) cross-section compared with ($n$, $\gamma_1$) is within a factor of ~ 1/30. Note that the example in Fig. 6 refers to the lower $C_W$ values. The tendency is as follows: an increase in $C_W$ leads to the increase of any cross-section, but the ($n$, $\gamma_0$) dominance remains within the above factor.

Summarizing our results for the total cross-sections in Figs. 4–6, we find that starting from $E_{\text{c.m.}}$ ≈ 10 keV and down to thermal energies, the cross-section increases by $10^3$ times from ~ 10 μb to ~ 5–10 mb. We assume this result is a prospective one for future experiments. At the same time, because the data of [17] are preliminary and not sufficiently informative, our discussions on the agreement between the experiment and MPCM calculations in Figs. 4, 5, and 6 are slightly premature.

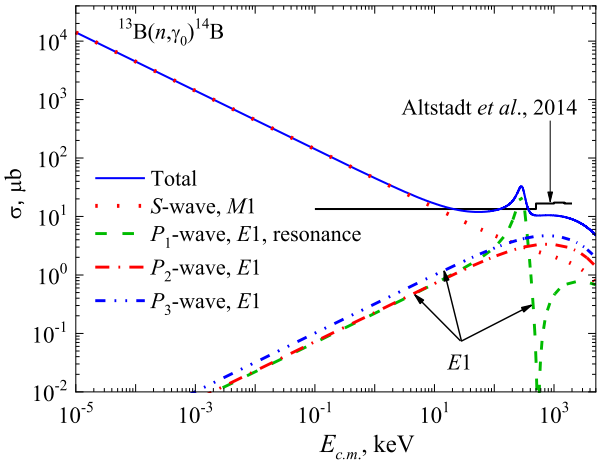


**Fig. 5.** (color online) Partial $E$1 and $M$1 and total cross-sections of $^{13}$B($n$, $\gamma_0$)$^{14}$B radiative capture to the GS of $^{14}$B ($C_W$ = 2.10 without FS). The histogram represents the experiment [17].

## IV. REACTION RATES OF RADIATIVE NEUTRON CAPTURE ON $^{10\text{-}13}$B AND $^{12\text{-}14}$C ISOTOPES

We follow [35] when calculating the reaction rate of radiative neutron capture. For the rate in units of cm$^3$mol$^{-1}$sec$^{-1}$, the following expression is used:

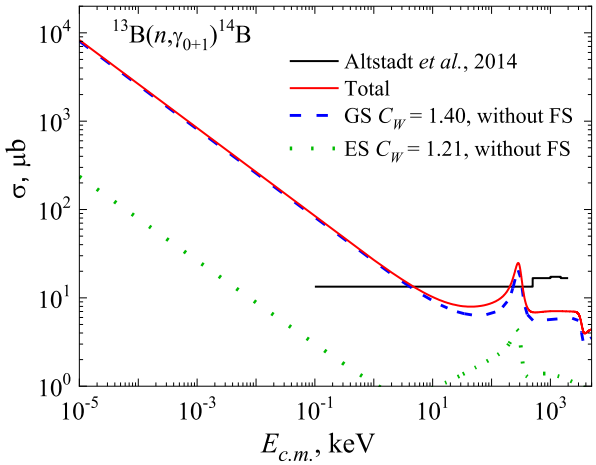


**Fig. 6.** (color online) Partial $E1$ and $M1$ and total cross-sections of $^{13}$B($n$, $\gamma_{0+1}$)$^{14}$B radiative capture to the ground $2^-$ and excited $1^-$ states of $^{14}$B ($C_W$ = 1.40 for the GS and $C_W$ = 1.21 for the ES). The histogram represents the experiment [17].

$$N_A\langle\sigma v\rangle = 3.7313\cdot 10^4 \mu^{-1/2} T_9^{-3/2} \int_0^\infty \sigma(E) E \times \exp(-11.605E/T_9)\mathrm{d}E, \quad (10)$$

where $N_A$ is Avogadro's number, $E$ is given in MeV, the total cross-section σ($E$) is in μb, $\mu$ is the reduced mass in amu, and $T_9$ is the temperature in $10^9$ K [35]. Appendix B illustrates the computational procedure accuracy of the reaction rate calculations.

### A. Reaction rate of neutron capture on $^{13}$B

In Fig. 7 (a), the red and blue solid curves show the ($n$,$\gamma_0$) capture reaction rates to the GS, which correspond to the results for the total cross-sections presented for the potentials without FS in Fig. 4 (b). The band in Fig. 7 (a) corresponds to the band in Fig. 4 and confines the possible reaction rate values for the range of $C_W$ discussed in Sec. II.B.

The black solid curve in Fig. 7 (a) shows the reaction rate from [8] obtained by Rauscher *et al*. Figure 7 (a) indicates that these results completely disregard the non-resonance part of the reaction, which leads to an increase in the cross-sections at low energies owing to the $M1$ transition, as shown in Fig. 4 (b) and Fig. 6.

An important remark concerns the structure of bound states. In [8], the $D$ component is assumed for both the GS and ES of $^{14}$B in the $n$ + $^{13}$B channel, in contrast with our treating these states as $S$-waves. Consequently, there are no $M1$ transitions in the calculations of Rauscher *et al*. [8], which provide the low-temperature reaction rate. The resonance structure of the black curve in Fig. 7 is due to the $3^-$ ($E_x$ = 1.38 MeV) resonance, and the $1^+$ resonance ($E_x$ = 1.275 MeV) is not considered. The signature of the $1^+$ (305 keV) resonance in the cross-sections in Figs. 4–6 incorporated in the current calculations is observed in reaction rates as an increase at temperatures of $T_9 \geq 0.2$ in Fig. 7.

Figure 7 (b) shows the input of the ($n$, $\gamma_1$) capture to the reaction rate through the example of one $C_W$ set. As shown in Fig. 6, the ($n$, $\gamma_1$) capture contribution of the excited $1^-$ state is relatively small, resulting in the values of the reaction rate in Fig. 7 (b) (red dotted curve). The same tendency is preserved for any other $C_W$ set.

The signature of the 300 keV resonance in the cross-sections in Figs. 4–6 is observed in the reaction rates as an increase at temperatures of $T_9 \geq 0.2$ in Fig. 7.

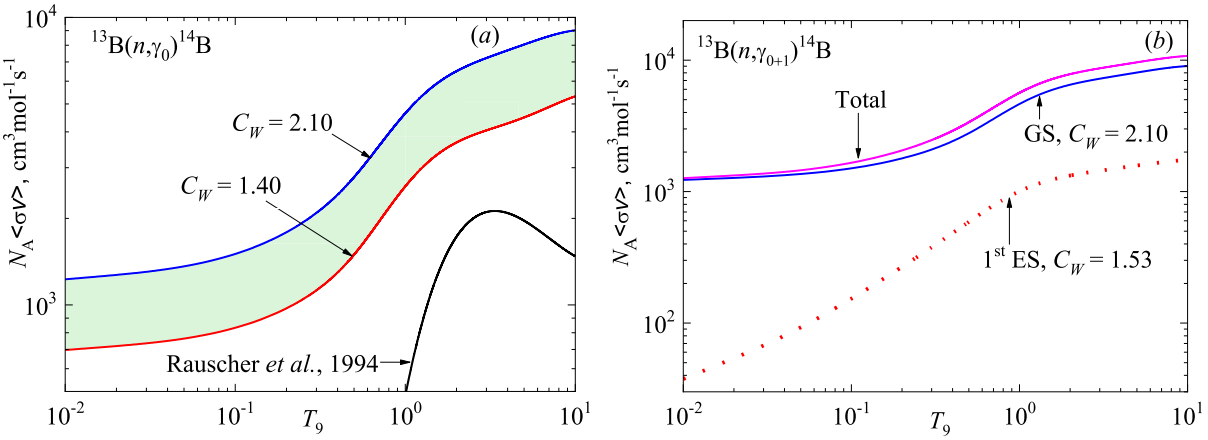


**Fig. 7.** (color online) Reaction rate of radiative neutron capture on $^{13}$B calculated with potentials without FS. (*a*) Transitions to the GS: potential No. 1 from Table 2 ($C_W$ = 1.40) – red solid curve, potential No. 3 from Table 2 ($C_W$ = 2.10) – blue solid curve. The black solid curve shows the reaction rate obtained by Rauscher *et al*. in Ref. [8]. (*b*) Transitions to the ground and excited states: GS potential No. 3 from Table 2 ($C_W$ = 2.10) – blue solid curve; ES potential No. 3 from Table 3 ($C_W$ = 1.53) – red dotted curve. The magenta solid curve is the total capture reaction rate.

The reaction rates in Fig. 7 are parameterized by an expression of the form [36]

$$N_A\langle\sigma v\rangle = a_1/T_9^{2/3}\exp(-a_2/T_9^{1/3})(1.0+a_3T_9^{1/3} + a_4T_9^{2/3}+a_5T_9+a_6T_9^{4/3}+a_7T_9^{5/3})+\frac{a_8}{T_9}. \quad (11)$$

The parameters $a_i$ given in Table 4 correspond to the reaction rates presented in Fig. 7: the first column refers to the red solid curve in Fig. 7 (a); the second column – the blue solid curve in Fig. 7 (a); the third column – the red dotted curve in Fig. 7 (b); the last column – the magenta solid curve in Fig. 7 (b).

The reaction rates are presented in Table A1 of Appendix A.

### B. Comparison of the neutron radiative capture rates on $^{10\text{-}13}$B and $^{12\text{-}14}$C isotopes

To define the role of the $^{13}$B($n$, $\gamma$ )$^{14}$B reaction in the boron chain of sequence in Fig. 1, we must consider whether the calculated reaction rates prove the formation of $^{14}$B or $^{13}$B decays before neutron capture may start. Short-lived isotopes may provide *r*-processes in an explosive environment and neutron-rich matter at high densities [37]. The conventional density –temperature conditions for the *r*-process are assumed as $\bar{n}_n \sim 10^{22} - 10^{23}$ cm$^{-3}$ and $T_9 \sim 1$ [2, 38]. We examine these conditions for the $^{13}$B($n$, $\gamma$)$^{14}$B reaction based on the calculated reaction rates.

We can identify the r-process according to the following relation:

$$\tau_\beta \approx N_n\tau(n,\gamma), \quad (12)$$

where the mean lifetime of $\beta$-decay $\tau_\beta$ and neutron capture time $\tau(n,\gamma)$ are interrelated by the number of neutrons $N_n$ that must be captured before $\beta$-decay occurs [37, 39]. The neutron capture time $\tau(n,\gamma)$ depends on the reaction rate and neutron number density $\bar{n}_n$ [40],

$$\tau(n,\gamma) = \frac{1}{\bar{n}_n\langle\sigma_{n,\gamma}v\rangle}. \quad (13)$$

Note that the recommended half-life values $t_{1/2}$ [18, 41, 42] span the range 17.10 – 17.52 ms, and following the Sargent formula $t_{1/2} = \tau_\beta\ln(2)$, the mean lifetime range is 0.0243 s < $\tau_\beta$ < 0.0253 s. Further calculations reveal minor variations within the $\tau_\beta$ interval.

The $\tau(n,\gamma)$ calculation results for the $^{13}$B($n$, $\gamma_0$)$^{14}$B reaction are shown in Fig. 8 (a) as an insert. The dashed line corresponds to the $^{13}$B mean lifetime $\tau_\beta$ = 0.0248 s and $\bar{n}_n = 10^{23}$ cm$^{-3}$.

The arrows indicate the equality $\tau_\beta = \tau(n,\gamma)$ and reflect the equilibrium of the decay and capture processes, $N_n$ = 1. The area under the dashed line holds $\tau(n,\gamma) < \tau_\beta$, which means that the number of neutrons that interact with $^{13}$B is $N_n > 1$, as shown in the main field of Fig. 8 (a). We may conclude that at temperatures of $T_9$ on the right of the arrows, the process ($n$, $\gamma$) is faster compared with $\beta$-decay. Therefore, the ignition of the $^{13}$B($n$, $\gamma_0$)$^{14}$B reaction occurs at $T_9 \geq 0.4$ in the case of the reaction rate shown by the upper curve ($C_W$ = 2.10) in Fig. 7 (a) and at $T_9 \geq 0.9$ in the case of the low red curve ($C_W$ = 1.40).

Figure 8 (b) shows the correlation between the variation in the neutron density and ignition temperature $T_9$, *i.e.*, for higher $\bar{n}_n$, a lower $T_9$ is needed to provide the number of ($n$, $\gamma_0$) capture acts $N_n > 1$.

Figure 8 (c) illustrates the same regularities, but we find a very specific feature. Fig. 7 (b) shows no essential input of the ($n$, $\gamma_1$) process, playing the role of reaction rate correction, but its inclusion when considering neutron capture time $\tau(n,\gamma_{0+1})$ leads to the noticeable shift in ignition points to the lower edge of the $T_9$ scale: $0.15T_9 \rightarrow 0.1T_9$ ($\bar{n}_n = 1.5\cdot10^{22}$ cm$^{-3}$); $0.4T_9 \rightarrow 0.3T_9$ ($\bar{n}_n$ =

**Table 4.** Parameters in (11) for the reaction rates in Fig. 7.

| $i$ | ($n$, $\gamma_0$), $C_W$ = 1.40 | ($n$, $\gamma_0$), $C_W$ = 2.10 | ($n$, $\gamma_1$), $C_W$ = 1.53 | ($n$, $\gamma_{0+1}$), $C_W$ = 2.10 and $C_W$ = 1.53 |
|---|---|---|---|---|
| | $a_i$ | $a_i$ | $a_i$ | $a_i$ |
| 1 | 14381.77 | 17240.08 | 2413.837 | 19795.34 |
| 2 | 1.41717 | 1.2962 | 1.46568 | 1.31492 |
| 3 | −2.61253 | −2.52512 | −3.81023 | −2.64425 |
| 4 | 1.16178 | 0.93077 | 4.53362 | 1.25477 |
| 5 | 3.19007 | 3.74616 | 2.12766 | 3.6103 |
| 6 | −2.58617 | −2.76411 | −2.80537 | −2.77072 |
| 7 | 0.57029 | 0.57636 | 0.69249 | 0.58652 |
| 8 | 4.74344 | 7.39244 | 0.13587 | 7.62151 |
| | $\chi^2$ = 0.13 | $\chi^2$ = 0.09 | $\chi^2$ = 0.12 | $\chi^2$ = 0.09 |

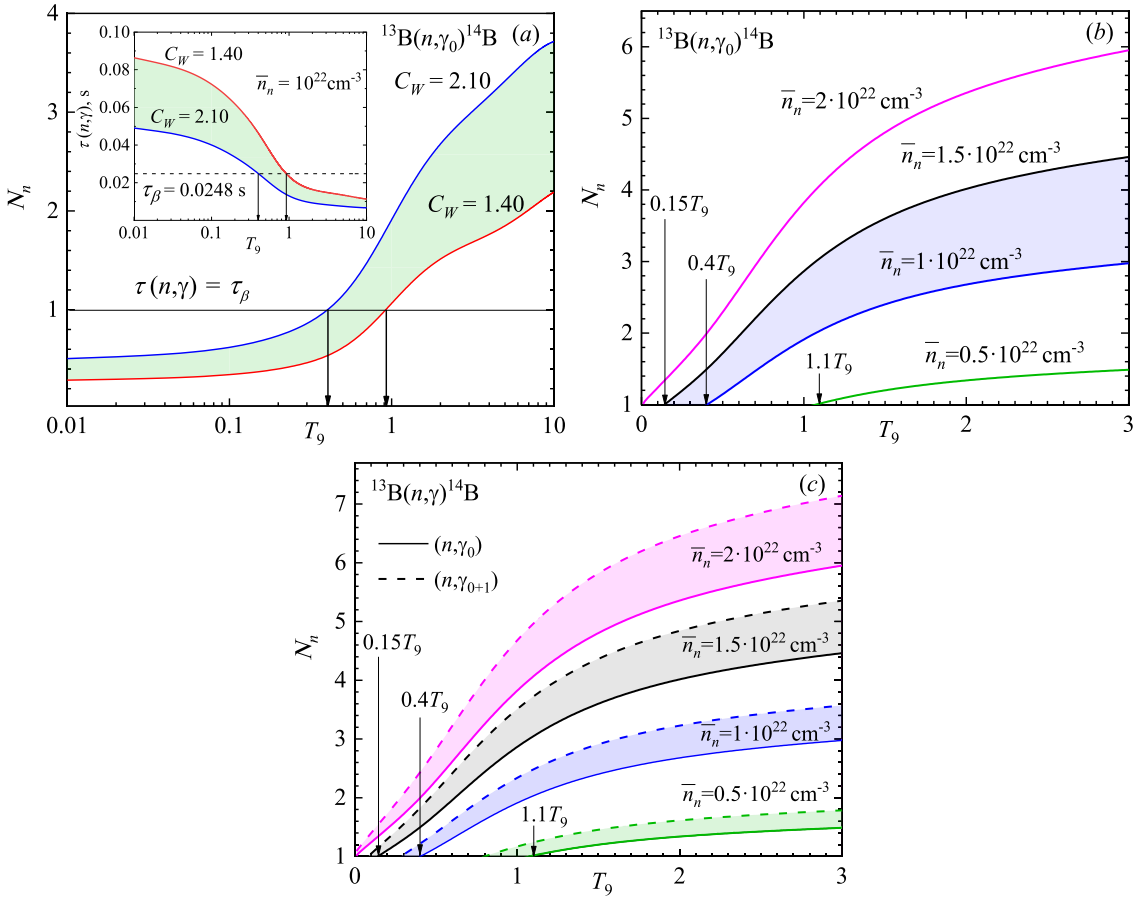


**Fig. 8.** (color online) Number of captured neutrons $N_n$ dependence on $T_9$ conditioned by the neutron number density $\bar{n}_n$. (*a*) $\bar{n}_n$= 10$^{22}$ cm$^{-3}$. The band corresponds to the reaction rates in Fig. 7. The insert shows the neutron capture time $\tau(n,\gamma)$.(*b*) Illustration of the ignition $T_9$ values depending on the neutron number density $\bar{n}_n$. (*c*) Effect of the excited state: solid curves correspond to ($n$, $\gamma_0$) capture to the GS; dashed curves correspond to the ($n$, $\gamma_{0+1}$) total capture.

$1\cdot10^{22}$cm$^{-3}$); $1.1T_9 \to 0.8T_9$ ($\bar{n}_n = 0.5\cdot10^{22}$cm$^{-3}$). Therefore, even a slight increase in reaction rate gives feedback to the occurrence of the $^{13}$B($n$, $\gamma_{0+1}$)$^{14}$B reaction. There are no temperature constraints at high neutron density $\bar{n}_n > 2\cdot10^{22}$.

The $T_9$ interval relevant to the start of the *r*-production of $^{14}$B may be defined at the present stage as $0.1 < T_9 < 0.8$ under neuron density matter conditions of $0.5\cdot10^{22}$ cm$^{-3}$ $< \bar{n}_n <$ $1.5\cdot10^{22}$ cm$^{-3}$. Based on these results, we compare the reaction rates of radiative neutron capture on $^{10\text{-}13}$B and $^{12\text{-}14}$C isotopes calculated within the same MPCM model formalism, as presented in Fig. 9.

It is natural that the production of isotopes with mass number $A$ following $A$-1 provides the continuation of the neutron-induced sequence if the previous reaction rate is comparable to or prevailed over by the next one. This regularity for the $^{10-13}$B isotopes is observed directly at temperatures of ~ 0.05 – 0.3$T_9$, which overlaps with the window for $^{14}$B production. The gaps at low and high $T_9$ in the case of the $^{11}$B($n$, $\gamma$)$^{12}$B reaction rate are not worrying because the isotope $^{11}$B is stable and may be accumu-

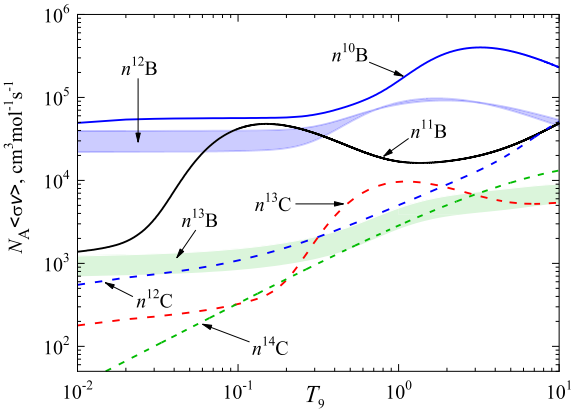


**Fig. 9.** (color online) Comparison of the neutron capture reaction rates on $^{10-13}$B and $^{12-14}$C isotopes calculated in the MPCM. $^{10}$B($n$,$\gamma$)$^{11}$B – blue solid curve [9], $^{11}$B($n$, $\gamma$)$^{12}$B – black solid curve [10, 11], $^{12}$B($n$, $\gamma$)$^{13}$B – pale blue band [12], $^{13}$B($n$, $\gamma$)$^{14}$B – pale green band (present calculations), $^{12}$C($n$, $\gamma$)$^{13}$C – blue dashed curve [13], $^{13}$C($n$, $\gamma$)$^{14}$C – red dashed curve [14], $^{14}$C($n$, $\gamma$)$^{15}$C – green dashed curve (unpublished). Additional details are provided in Table 5.

lated.

We now complement the comparative analysis of the boron chain with information from Table 5. A correlation between the threshold energies $E_{\rm th}$ in the boron channels and the reaction rates at ultra-low $T_9$ is observed, *i.e.*, a higher $E_{\rm th}$ results in a higher reaction rate. The thermal cross-sections for odd-odd $^{10,12}$B isotopes are nearly an order larger than $\sigma_{\rm therm}$ of the odd-even $^{11,13}$B. We can observe these relationships for the reaction rates in Fig. 9, except at the temperature interval ~ 0.02 – 1$T_9$ for the $^{11}$B($n$, $\gamma_{0+1+2+3+4}$)$^{12}$B reaction, where the rate essentially increases owing to the large number of resonances in this channel. Moreover, the calculated $\sigma_{\rm therm}$ for $^{11}$B($n$, $\gamma$)$^{12}$B shows excellent agreement with the measured value (see details in Refs. [10, 11]), and we interpret this result as the substantiation of the obtained $\sigma_{\rm therm}$ for $^{13}$B($n$, $\gamma$)$^{14}$B in this study.

The isobar-analog channels $^{13}$B($n$, $\gamma$)$^{14}$B and $^{13}$C($n$, $\gamma$)$^{14}$C lead to the formation of $^{14}$C either via $^{14}$B $\beta$-decay or direct radiative neutron capture on $^{13}$C. Fig. 9 shows that at temperatures below 0.3$T_9$, the boron channel rate exceeds the carbon one and decreases in the range ~ 0.3 – 3$T_9$, and at $T_9 > 3$, the reaction rates in both channels become close. Consequently, we may conclude that both $^{14}$C production processes exhibit comparable efficiency.

## V. CONCLUSION

The total cross sections of the $^{13}$B($n$, $\gamma_{0+1}$)$^{14}$B reaction are calculated in the MPCM based on the $E1$ and $M1$ transitions from $10^{-2}$ eV to 5 MeV. We prove that the strong sensitivity of the cross sections to the asymptotic constant $C_W$ provides an appropriate long-range dependence of the radial bound $S$ wave functions; thus, a larger $C_W$ results in larger absolute values of cross-sections. The role of the FS in the calculated spectrum turned out to be insignificant.

The $E1$ transitions provides the background of the cross-section owing to the capture from the non-resonance $^{3+5}P_2$, $^{5}P_3$, and $^{3}P_0$ waves, and the resonant $^{3+5}P_1$ wave in the initial channel reveals the resonance structure of the cross-section at ~ 300 keV.

The $M1$ transition occurs via the $S$ scattering wave and contributes predominantly to the thermal cross-sections. The variation in $C_W$ = 1.4 – 2.4 gives the range of $\sigma_{\rm therm}$ = 5.1 – 8.9 mb. These $\sigma_{\rm therm}$ values have not ever been estimated in theory, which may be important for researchers.

The reaction rates of the $^{13}$B($n$, $\gamma_{0+1}$)$^{14}$B process exhibit the same dependence on the asymptotic constant $C_W$ and the relative contributions of the ($n$, $\gamma_0$) and ($n$, $\gamma_1$) channels. The results of MPCM calculations differ cardinally from those of Rauscher *et al.* [8] across the entire $T_9$ range. Therefore, we conclude that the present data on the reaction rates substantiate the role of the $^{13}$B($n$, $\gamma_{0+1}$)$^{14}$B reaction in boron-carbon-nitrogen chains, *i.e.*, this is not the break-point of the boron sequence.

To support our conclusion, we estimate the relationship between the mean lifetime of $^{13}$B $\beta$ decay $\tau_\beta$ and neutron capture time $\tau(n,\gamma)$. The temperature window for the ignition of $^{14}$B $r$-production, 0.1 – 0.8$T_9$, related to the neutron densities $\bar{n}_n$= 5 $10^{21}$ – 1.5 $10^{22}$ cm$^{-3}$ is determined, whereas at $\bar{n}_n$> 1.5 $10^{22}$ cm$^{-3}$, there are no temperature limits. We demonstrate that the preferences for the $^{13}$B($n$, $\gamma_{0+1}$)$^{14}$B reaction directly depend on the reaction rate values; the larger the $\langle\sigma_{n,\gamma}v\rangle$values, the shorter the neutron capture time $\tau(n,\gamma)$.

We foresee the following factors increasing the reaction rate. The inclusion of the $D$-component into the bound GS (its weight is estimated today at ~ 17%) may enhance the input of the $1^+$ resonance to the $E1$ capture cross-section at 305 keV. The role of the transitions shown inFig. 2 but not considered in the present study may be evaluated; as an example, the inclusion of a rather weak ($n$, $\gamma_1$) process leads to the narrowing of the ignition temperature interval. Another problem concerns the determination of $3^\pi$ level parity at $E_x$ = 4.06 MeV. If $\pi$ = +1, the additional $E1$ transition may occur. In the case of $\pi$ = −1, the $E2$ transition may reveal interference effects with the $3^-$ state at $E_x$ = 1.38 MeV.

The unique experimental results on the Coulomb dissociation of $^{14}$B [17], converted into the cross-section of the $^{13}$B($n$, $\gamma$)$^{14}$B reaction, remain preliminary and are not complete with estimated uncertainties.

**Table 5.** Overview of radiative neutron capture reactions on $^{10-13}$B and $^{12-14}$C isotopes calculated in the MPCM.

| Reaction | Threshold energy $E_{\rm th}$/MeV | Included bound states | Included resonances | $\sigma_{\rm therm}$/mb | Ref. |
|---|---|---|---|---|---|
| $^{10}$B($n$,$\gamma$)$^{11}$B | 11.4541 | ($n$,$\gamma_{0+2+3+4+9}$) | $^{6+8}P_{5/2}$, $^{6+8}D_{5/2}$, $^{6+8}D_{7/2}$ | 405 | [9] |
| $^{11}$B($n$,$\gamma$)$^{12}$B | 3.3700 | ($n$,$\gamma_{0+1+2+3+4}$) | $^{3+5}P_2$, $^{3+5}D_1$(I), $^{3+5}D_2$, $^{3+5}D_3$, $^{3+5}D_1$(II), $^{5}F_1$(I), $^{3+5}F_3$(I), $^{5}F_1$(II) | 10.6 | [10,11] |
| $^{12}$B($n$,$\gamma$)$^{13}$B | 4.8780 | ($n$,$\gamma_0$) | $^{4}D_{1/2}$, $^{4}D_{5/2}$, $^{4}P_{5/2}$ | 176 and 285 | [12] |
| $^{13}$B($n$,$\gamma$)$^{14}$B | 0.9700 | ($n$,$\gamma_{0+1}$) | $^{3+5}P_1$ | 5.1 – 8.9 | present |
| $^{12}$C($n$,$\gamma$)$^{13}$C | 4.9464 | ($n$,$\gamma_{0+1+2+3}$) | $^{2}D_{3/2}$ | 3.4 – 3.9 | [13] |
| $^{13}$C($n$,$\gamma$)$^{14}$C | 8.1765 | ($n$,$\gamma_{0+1+2}$) | $^{2}P_{1/2}$ | 1.50 | [14] |
| $^{14}$C($n$,$\gamma$)$^{15}$C | 1.2181 | ($n$,$\gamma_{0+1}$) | $^{2}P_{3/2}$ | $5\cdot10^{-6}$ | – |

We assume that our results on the reaction rate of $^{13}B(n, \gamma)^{14}B$ may change the perspective expressed in Ref. [7] on its minor impact on heavy element production. The present calculations are predictive and estimative to substantiate the performance of new experiments on the neutron capture on $^{13}B$ and give a model estimation of the reaction rate of the synthesis of the $^{14}B$ isotope in the $n^{13}B$ channel for the first time.

## APPENDIX A

### Radiative capture reaction rates

**Table A1.** $^{13}B(n, \gamma)^{14}B$ radiative capture reaction rates.

| $T_9$ | $(n, \gamma_0)$, $C_W = 1.40 N_A \langle\sigma v\rangle$ | $(n, \gamma_0)$, $C_W = 2.10 N_A \langle\sigma v\rangle$ | $(n, \gamma_1)$, $C_W = 1.53 N_A \langle\sigma v\rangle$ | $(n, \gamma_{0+1})$, $C_W = 2.10$ and $C_W = 1.53 N_A \langle\sigma v\rangle$ |
|---|---|---|---|---|
| 0.01 | 696.895 | 1227.53 | 37.5176 | 1265.0476 |
| 0.02 | 718.923 | 1270.56 | 53.8965 | 1324.4565 |
| 0.03 | 734.56 | 1302.34 | 67.2893 | 1369.6293 |
| 0.04 | 749.033 | 1332.05 | 80.0969 | 1412.1469 |
| 0.05 | 763.127 | 1361.07 | 92.6427 | 1453.7127 |
| 0.06 | 777.063 | 1389.77 | 105.014 | 1494.784 |
| 0.07 | 790.928 | 1418.33 | 117.244 | 1535.574 |
| 0.08 | 804.764 | 1446.79 | 129.351 | 1576.141 |
| 0.09 | 818.593 | 1475.22 | 141.346 | 1616.566 |
| 0.1 | 832.43 | 1503.63 | 153.236 | 1656.866 |
| 0.2 | 972.988 | 1789.64 | 267.522 | 2057.162 |
| 0.3 | 1123.68 | 2088.81 | 376.527 | 2465.337 |
| 0.4 | 1296.14 | 2417.88 | 483.691 | 2901.571 |
| 0.5 | 1496.05 | 2783.22 | 589.108 | 3372.328 |
| 0.6 | 1717.03 | 3173.33 | 690.019 | 3863.349 |
| 0.7 | 1946.46 | 3568.69 | 783.394 | 4352.084 |
| 0.8 | 2172.32 | 3951.72 | 867.368 | 4819.088 |
| 0.9 | 2386.04 | 4310.64 | 941.37 | 5252.01 |
| 1 | 2582.75 | 4639.3 | 1005.75 | 5645.05 |
| 1.5 | 3291.73 | 5830.41 | 1217.32 | 7047.73 |
| 2 | 3672.32 | 6500.93 | 1325.54 | 7826.47 |
| 2.5 | 3894.09 | 6920.42 | 1392.2 | 8312.62 |
| 3 | 4046.34 | 7223.52 | 1441.32 | 8664.84 |
| 3.5 | 4169.1 | 7469.1 | 1481.95 | 8951.05 |
| 4 | 4279.75 | 7682.51 | 1517.62 | 9200.13 |
| 4.5 | 4385.5 | 7874.58 | 1549.74 | 9424.32 |
| 5 | 4488.98 | 8049.78 | 1578.96 | 9628.74 |
| 6 | 4690.21 | 8355.32 | 1629.74 | 9985.06 |
| 7 | 4879.33 | 8603.13 | 1671.11 | 10274.24 |
| 8 | 5049.62 | 8794.33 | 1703.62 | 10497.95 |
| 9 | 5196.07 | 8931.47 | 1727.77 | 10659.24 |
| 10 | 5316.06 | 9018.76 | 1744.08 | 10762.84 |
| | $\chi^2 = 0.13$ | $\chi^2 = 0.09$ | $\chi^2 = 0.12$ | $\chi^2 = 0.09$ |

## APPENDIX B

### Evaluation of the reaction rate within the computational procedures

To assess reaction rate calculation accuracy, we evaluate the impact of the integration parameters on the calculated reaction rate (10). In addition, we study the influence of the integration method. The integration options we consider are the Simpson method (second order, $m$ = 2) [43] and Milne method (fourth order, $m$ = 4) [44].

Figure B1 shows the effect of changing $E_{max}$ from 1 to 7 MeV at a constant step $E_{step}$ = 0.25 keV using the Simpson method (panel *a*), and the dependence of the reaction rate on $E_{step}$ varies from 0.1 keV to 1 keV at a constant $E_{max}$ = 5 MeV (panel *b*).

When changing $E_{max}$, the shape of the reaction rate at high temperatures does not practically change at $E_{max} \geq 4$ MeV. In the region of low temperature at $E_{step} \leq 0.25$ keV, the shape of the reaction rate is virtually unchanged. In this study, we assume $E_{max}$ = 5 MeV and an integration step $E_{step}$ of 0.25 keV.

We also test the Milne method [44] with a uniform grid, assuming $E_{min}$ = 0, the next point is at the first step of energy integration, and $E_{max}$ = 4 MeV. Figure B1 (b) shows the results at $E_{step}$ = 1 keV (red dashed curve) and $E_{step}$ = 0.25 keV (blue dotted curve). At $E_{step}$ = 0.25 keV, the calculation result does not depend on the method for calculating the integral of the reaction rate, but Milne's method works faster.

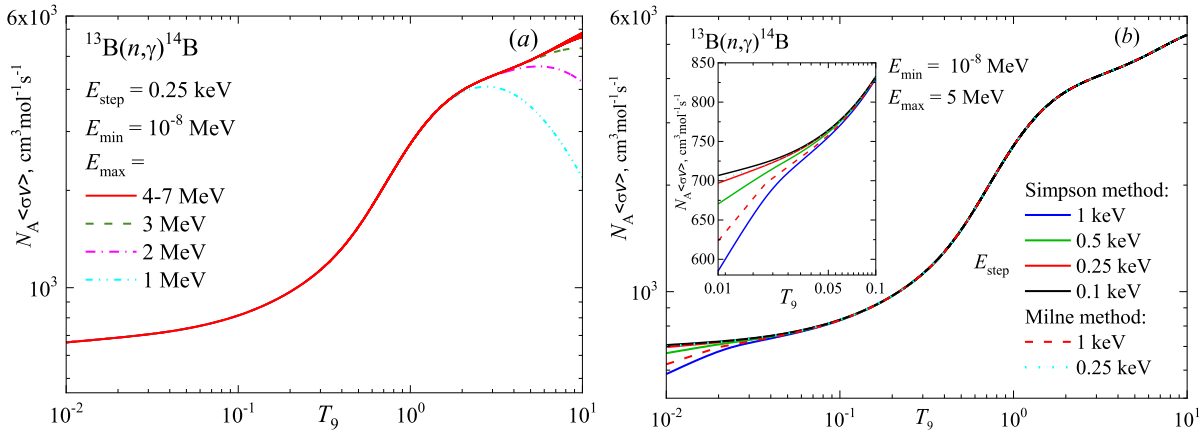


**Fig. B1.** (color online) Dependence of the shape of the reaction rate on the integration procedure in expression (10). The lower integration limit $E_{min} = 10^{-8}$ MeV. (*a*) Variation in $E_{max}$ in the range of 1 MeV to 7 MeV at a constant $E_{step}$ = 0.25 keV calculated using the Simpson method. (*b*) Variation in $E_{step}$ in the range of 0.1 keV to 1 keV at a constant $E_{max}$ of 5 MeV calculated using the Simpson and Milne methods.

## References


[1] M. Arnould and S. Goriely, Prog. Part. Nucl. Phys. , **112**, 103766 (2020)
[2] T. Kajino, W. Aoki, A. B. Balantekin, *et al.*, Prog. Part. Nucl. Phys. **107**, 109-166 (2019)
[3] R. Chatterjee and M. Dan, J. Astrophys. Astron. , **41**, 51 (2020)
[4] T. Kajino, G. J. Mathews, and G. M. Fuller, Astrophys. J. , **364**, 7 (1990)
[5] T. Kajino, Nucl. Phys. A. , **588**, C339-C343 (1995)
[6] M. Terasawa, K. Sumiyoshi, T. Kajino *et al.*, Astrophys. J. , **562**, 470-479 (2001)
[7] T. Sasaqui, T. Kajino, G. J. Mathews *et al.*, Astrophys. J. , **634**, 1173-1189 (2005)
[8] T. Rauscher, J. H. Applegate, J. J. Cowan *et al.*, Astrophys. J. , **429**, 499 (1994)
[9] S. B. Dubovichenko, N. A. Burkova, and A. V. Dzhazairov-Kakhramanov, Nucl. Phys. A. , **992**, 121625 (2019)
[10] S. B. Dubovichenko, N. A. Burkova, A. V. Dzhazairov-Kakhramanov *et al.*, Astropart. Phys. , **123**, 102481 (2020)
[11] S. B. Dubovichenko, N. A. Burkova, A. S. Tkachenko *et al.*, Int. J. Mod. Phys. E **32**, 23500088 (2023)
[12] S. B. Dubovichenko, N. A. Burkova, A. V. Dzhazairov-Kakhramanov *et al.*, Nucl. Phys. A. , **1011**, 122197 (2021)
[13] S. B. Dubovichenko and N. A. Burkova, Russ. Phys. J. , **64**(2), 216-227 (2021)
[14] S. B. Dubovichenko, Russ. Phys. J. , **65**, 208-215 (2022)
[15] S. Dubovichenko, A. Dzhazairov-Kakhramanov, N. Afanasyeva, Int. J. Mod. Phys. E. , **22**, 1350075 (2013)
[16] Y. Nagai, M. Kinoshita, M. Igashira *et al.*, Phys. Rev. C. , **102**, 044616 (2020)
[17] S. G. Altstadt, T. Adachi, Y. Aksyutina *et al.*, Nucl. Data Sheets, **120**, 197-200 (2014)
[18] Sukhoruchkin S. I. , Supplement to I/25 A-F (Springer Berlin Heidelberg, 2016)
[19] F. Ajzenberg-Selove, Nucl. Phys. A. , **523**, 1-196 (1991)
[20] S. B. Dubovichenko, A. S. Tkachenko, R. Ya. Kezerashvili

*et al*., Phys. Rev. C, **105**, 065806 (2022)
[21] S. Dubovichenko, B. Yeleusheva, N. Burkova *et al*., Chinese Phys. C, **47**, 084105 (2023)
[22] S. B. Dubovichenko, *Radiative neutron capture: Primordial nucleosynthesis of the universe* (Berlin: De Gruyter, 2019) p. 310
[23] S. B. Dubovichenko, *Thermonuclear processes in Stars and Universe*, Fourth Russian Edition (Saarbrucken: Scholar's Press, 2019), p. 332
[24] CODATA, (2010), https://pml.nist.gov/cuu/Constants/index.html, retrieved 04 April 2023
[25] V. Varlamov, B. Ishkhanov, and S. Yu, (2015), http://cdfe.sinp.msu.ru/services/ground/NuclChart_release.html , retrieved 18 February 2023
[26] I. V. Kurdyumov, Yu. F. Smirnov, K. V. Shitikova *et al*., Nucl. Phys. A. , **145**, 593-612 (1970)
[27] A. Volya and Yu. M. Tchuvil'sky, Phys. Rev. C. , **91**, 044319 (2015)
[28] V. I. Kukulin, V. G. Neudatchin, I. T. Obukhovski *et al*., Clust. as Subsystems Light Nucl. **3**, 1 (1983)
[29] V. Guimaraes, Brazilian J. Phys. , **34**, 1012-1016 (2004)
[30] S. Bedoor, A. H. Wuosmaa, J. C. Lighthall *et al*., Phys. Rev. C, **88**, 011304 (2013)
[31] V. Guimarães, J. J. Kolata, D. Bazin *et al*., Phys. Rev. C. , **61**, 064609 (2000)
[32] S. B. Dubovichenko and A. V. Dzhazairov-Kakhramanov, Phys. Part. Nucl. , **28**, 615-641 (1997)
[33] A. Estradé, R. Kanungo, W. Horiuchi *et al*., Phys. Rev. Lett., **113**, 132501 (2014)
[34] V. G. Neudatchin, V. I. Kukulin, V. N. Pomerantsev *et al*., Phys. Rev. C. , **45**, 1512-1527 (1992)
[35] C. Iliadis, *Nuclear physics of stars,* Second Edition (Weinheim, Germany: Wiley-VCH Verlag GmbH & Co. KGaA, 2015), p. 672
[36] G. R. Caughlan and W. A. Fowler, At. Data Nucl. Data Tables, **40**, 283-334 (1988)
[37] T. Rauscher, *Essentials of Nucleosynthesis and Theoretical Nuclear Astrophysics* (IOP Publishing, 2020), ISBN: 978-0-7503-1149-6
[38] C. A. Bertulani and T. Kajino, Prog. Part. Nucl. Phys. , **89**, 56-100 (2016)
[39] T. Rauscher, Eur. Phys. J. A, **58**, 214 (2022)
[40] E. B. Norman and D. N. Schramm, Astrophys. J. , **228**, 881-892 (1979)
[41] NuDat Database, https://www.nndc.bnl.gov/nudat3/, retrieved 25 March 2023
[42] Nuclear Data Evaluation Project, https://nucldata.tunl.duke.edu/nucldata/GroundStatedecays/14B.shtml, retrieved 04 April 2023
[43] QTS2D program, http://num-anal.srcc.msu.ru/lib_na/cat/q/qts2r.htm, retrieved 04 January 2023
[44] G. Dahlquist and Å. Björck, *Numerical Methods in Scientific Computing*, (Philadelphia, PA, USA:SIAM, 2008), vol. 1